Progress in the Understanding and the Performance of Electron Cyclotron Heating and Plasma Shaping on TCV

J.-M. Moret 1), S. Alberti 1), Y. Andrèbe 1), K. Appert 1), G. Arnoux 1), R. Behn 1), Y. Camenen 1), S. Cirant 2), R. Chavan 1), S. Coda 1), I. Condrea 1), A. Degeling 1), B.P. Duval 1), D. Fasel 1), A. Fasoli 1), F. Gandini 2), T.P. Goodman 1), M. Henderson 1), J.-P. Hogge 1), J. Horacek 1), P.F. Isoz 1), B. Joye 1), A. Karpushov 1), I. Klimanov 1), P. Lavanchy 1), J.B. Lister 1), X. Llobet 1), J.-C. Magnin 1), B. Marletaz 1), P. Marmillod 1), Y. Martin 1), A. Martynov 1), J.-M. Mayor 1), A. Mück 1), P. Nikkola 1), S. Nowak 2), P.J. Paris 1), I. Pavlov 1), A. Perez 1), R.A. Pitts 1), A. Pochelon 1), L. Porte 1), F. Ryter 3), O. Sauter 1), A. Scarabosio 1), M. Siegrist 1), U. Siravo 1), A. Sushkov 4), G. Tonetti 1), M.Q. Tran 1), H. Weisen 1), M. Wischmeier 1), A. Zabolotsky 1), G. Zhuang 1)

1) Centre de Recherches en Physique des Plasmas, Association EURATOM - Confédération Suisse, École Polytechnique Fédérale de Lausanne, CRPP-EPFL, CH-1015 Lausanne, Switzerland
2) Istituto di Fisica del Plasma, Euratom-ENEA-CNR Association, Milano, Italy
3) Max Planck Institut für Plasmaphysik, Euratom Association, Boltzmannstrasse 2, D-85748 Garching, Germany
4) Russian Research Centre, Kurchatov Institute, 123182 Moscow, Russia

e-mail contact of main author: jean-marc.moret@epfl.ch

Abstract. Powerful ECH with an adaptable launching geometry and plasma shaping capability are exploited on TCV to create and control high performance regimes, with 3 MW of 2nd and 1.5 MW of 3rd harmonic (X3) and real time optimisation of the absorption by mirror feedback. Full X3 absorption with launching parallel to the resonant surface was obtained. Electron temperature profile stiffness was measured as a function of the shape up for a large range of temperature gradients and confirmed that the diffusivity is lower at negative triangularity and high elongation. The link between shear and transport was verified by interleaved modulation of co- and counter-ECCD. ECCD efficiency and fast electron generation and transport measurements demonstrate the role of transport on the driven current profile. Stationary electron ITBs were created and the role of the current profile in transport reduction was clarified by improving or destroying the barrier with a small induced electric field.

1. Introduction

Powerful electron cyclotron heating (ECH) with a highly adaptable launching geometry and plasma shaping capability make the TCV tokamak (Tokamak à Configuration Variable) a unique tool to address a number of crucial research areas for the next generation burning plasma experiments and for the improvement of the tokamak concept. One challenge for TCV is the achievement and control of high performance regimes with sustained increased energy confinement properties, exempt from macroscopic instabilities, in dominant electron heating and low collisionality to simulate the conditions generated by α-heating in a reactor plasma. Local modifications in the pressure and current distributions involving external heat and current sources together with tuning in the main plasma shape and divertor configuration are required for the creation and optimisation of these regimes. Both methods are exploited on TCV. Its ECH and current drive (ECCD) system amounts to a total power of up to 4.5 MW, 3 MW at the second harmonic (X2) and 1.5 MW at the third harmonic (X3). The flexibility in the launching geometry, that was privileged during the design of the system, is now complemented with a real time optimisation of the wave absorption using an appropriate feedback on the mirror angles. This results in an unsurpassed power density with a precise control of the location and extent of the power deposition region that is specific to ECH systems.

This overview presents recent developments on the understanding of the plasma-wave interaction at high ECH and ECCD power level as well as studies of fundamental plasma phenomenology such as electron heat transport. Based on this knowledge significant progress in the performance of advanced operational regimes has been achieved and is also reported.

Birth distribution of the resonant fast electrons and their diffusion due to transport have been experimentally determined with perturbative techniques. These observations show that collisional diffusion in velocity space and cross-field transport operate on comparable time scales and that the latter plays a key role in determining the driven current profile and the ECCD efficiency. (Section 2.)

It was possible to extend the range of one key parameter for the electron energy transport, the normalised electron temperature gradient, by a factor four compared to the highest value obtained on other tokamaks. This was performed using off-axis heating at the high power density available. In these conditions the stiffness of the electron temperature profile and the associated heat diffusivity as a function of the plasma triangularity were investigated. It is observed that the lowest heat diffusivity is obtained with the most negative triangular shapes. (Section 3.)

The link between the local magnetic shear and the anomalous electron transport was experimentally tested by a local modulation of the plasma current profile obtained by interleaving co and counter off-axis modulated ECCD with a constant total power. The modulation in the heat diffusivity due to the change in the magnetic shear appears as a localised source term in the electron temperature dynamical response and typical signatures for such a term are observed on the amplitude and phase profile of the temperature response. (Section 4.)

Stationary electron internal transport barriers (eITB) have been created both in fully ECCD driven discharges or with a residual inductive current component using a combination of off-axis co-ECCD to broaden the current channel and centrally absorbed ECH or counter-ECCD to control the depth of the central current trough and thus the strength of the barrier. Several properties of the eITB have been studied. Its formation, observed to occur in less than 1 ms, is considerably faster than the current diffusion time and comparable to the energy confinement time. The role of the current profile in the creation of the barrier was clarified by applying to a fully ECCD driven discharge a small electric field, corresponding to a negligible ohmic power of 3 kW. This electric field, due to the electrical conductivity profile, induces a centrally peaked current density which in the counter direction further enhances the barrier strength, while in the co-direction weakens or even destroys the barrier. (Section 5.)

Third harmonic ECH opens the possibility to heat plasmas with densities above the X2 cut-off. Vertically launched X3 waves propagating parallel to the resonant surface are used and a real time optimisation of the wave absorption in which the mirror angle tracks the maximum in the absorption curve was developed. Experimental measurements of X3 absorption were performed to validate ray/beam-tracing codes and full Fokker-Planck modelling. Injecting 1.35 MW of X3-ECCD into an ELMy H-mode ohmic target gave access to a new ELM regime in which the ELM frequency is decreased and the energy released by each ELM increased by a factor 10 compared to the ohmic case. (Section 6.)

The threshold power for L to H-mode transition using X2 heating was determined at densities below the X2 cut-off. This is found to be higher than the lowest threshold obtained in ohmic conditions at higher densities. It was also demonstrated that in these conditions, X3 heating with a similar power level can be used to assist the transition. (Section 7.)

2. Dynamics of suprathermal electron generation and transport

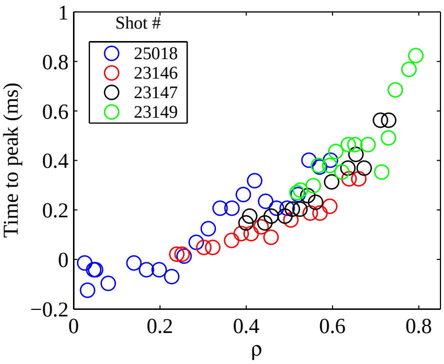

FIG. 1. Time lag from the end of a central ECCD pulse to the ECE peak, as a function of ρ_V *(normalised radial coordinate proportional to the square root of the plasma volume), calculated by taking into account the estimated relativistic down-shift (plasma current 230kA, density* $1.5\text{-}2.1\times10^{19}\,m^{-3}$*, electron temperature 1.5keV, elongation 1.6, power 0.45-0.9MW).*

The physics of ECCD is largely determined by the relaxation phenomena governing the behaviour of suprathermal electrons. In the past few years, a combination of quasi-linear modelling and direct experimental measurements in TCV has shown in particular that cross-field transport of suprathermal electrons plays a pivotal role in regulating the current profile and, in the uniquely high-power conditions of TCV, the ECCD efficiency as well [1]. In recent experiments [2] we have sought to probe the suprathermal (ECE) electron dynamics by studying the response of high field side (HFS) electron cyclotron emission to short, low duty cycle, periodic, localised ECCD pulses. The pulses are applied with one or two 0.45MW sources (with identical aiming) and are defined by a 0.2ms ramp-up, a 0.25ms flat top and a 0.1ms ramp-down, with a periodicity of 8 to 10ms. The measurement is performed with a second harmonic X-mode ECE radiometer, operating in the 78-114GHz range with 24 channels of 0.75GHz bandwidth [3], with coherent averaging applied over up to 200 pulses, resulting in a good signal-to-noise ratio in spite of a low (<40kW) average power. In order to extract quantitative information on the suprathermal population, we have employed the simple model of a bi-Maxwellian energy distribution, with uniform suprathermal temperature; this temperature can then be estimated from the relativistic shift of the spatial symmetry point of the signal distribution, as well as from equating the pulse decay time with the collisional slowing-down time. The optical thickness, thus ultimately the density, of the suprathermal population can then be derived from the radiative temperature through known formulas (note that the suprathermal population is invariably optically thin).

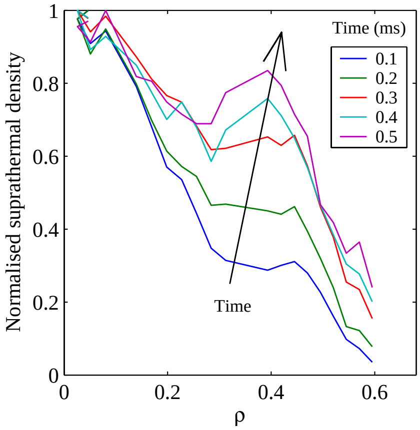

FIG. 2. Successive snapshots of normalised suprathermal density after on-axis ECCD turn-on ($t = 0s$*).*

The time to peak, calculated from the power turn-off time, is shown in Figure 1 as a function of minor radius, as a composite over several shots, with central heating in all cases. The overlapping data are in satisfactory agreement, with most of the scatter attributed to density variations. Ray tracing calculations place the ECH deposition in the region $\rho = 0-0.2$, which is confirmed by the measurements to be a region of zero delay, within the ECE time resolution of 0.05ms. The effect of radial transport on the shape of the suprathermal profile is evidenced by the successive snapshots of the normalised suprathermal density profile after power switch on, shown in Figure 2. A substantial broadening of the profile around the deposition region is clearly observed. While quantitative details can be strongly affected by the approximations inherent in our simple model, model-independent analysis techniques, such as System Identification techniques, have also been applied in order to determine the characteristic relaxation times and the power deposition profile. Initial results suggest that the latter is anomalously broad in the presence of significant cw ECH power. Further studies are planned to test this conclusion.

3. Influence of the shape on electron temperature stiffness and thermal diffusivity

FIG. 3. Electron heat flux versus electron temperature gradient at $\rho_V = 0.5$ *(normalised radial coordinate proportional to the square root of the plasma volume) for various triangularities.*

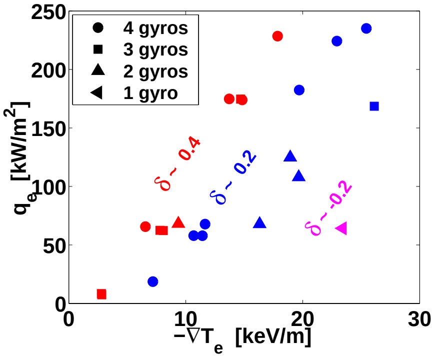

Electron heat transport investigations have been performed in L-mode plasmas [4][5] at plasma triangularities between -0.2 and +0.4, using spatially localised central and off-axis ECH to independently vary the electron temperature, T_e and its normalised gradient, R/L_{T_e}, where $L_{T_e} = \nabla T_e/T_e$. Because of the large power density installed, an unusually large range of values for R/L_{T_e} and for the heat flux, q_e was obtained. Figure 3 shows that at constant heat flux, larger gradients and thus better confinements are generated at lower or negative triangularity, as for the case of ohmic or centrally heated plasmas [6][7]. A strong dependence of the electron heat diffusivity, χ_e on T_e is observed, Figure 4. For the three points with the lowest χ_e, the TEM are calculated to be stable. There is no such clear dependence of χ_e observed on R/L_{Te} or R/L_{ne}, in contrast to the results from local gyro-fluid simulations (GLF23) [8].

FIG. 4. Electron heat diffusivity versus electron temperature at $\rho_V = 0.5$ *for various triangularities.*

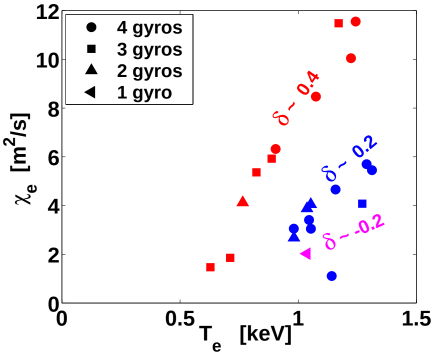

The experimental values of heat diffusivity are compared in Figure 5 to the predictions from the critical gradient model [9] for TCV and ASDEX-Upgrade. TCV data extends over a wider range of R/L_{T_e} and indicates also a strong dependence on triangularity.

The micro-instabilities responsible for the anomalous electron heat transport in these plasmas are determined using the local gyro-fluid (GLF23) and global collisionless gyro-kinetic linear simulations (LORB5). Ion temperature gradient (ITG) and trapped electron modes (TEM) are found to be unstable. The TEM are the most unstable modes, except at the lowest R/L_{T_e} values where they are stabilised and where ITG modes dominate. In all these plasmas, the high $Z_{eff}T_e/T_i$ values lead to complete stabilisation of the electron temperature gradient (ETG) modes. The plasma collisionality ν_{eff} is found to strongly reduce the electron heat transport, which is consistent with the stabilisation of TEM with increasing ν_{eff} in the simulations. However, the variation of ν_{eff} with δ in the experimental data prevents us to quantify the intrinsic dependence of χ_e on δ.

FIG. 5. Inter-machine comparison of gyro-Bohm normalised heat conductivity versus normalised temperature gradient at $\rho_V = 0.5$: ASDEX Upgrade (green), TCV at three different triangularities (red, blue, magenta).

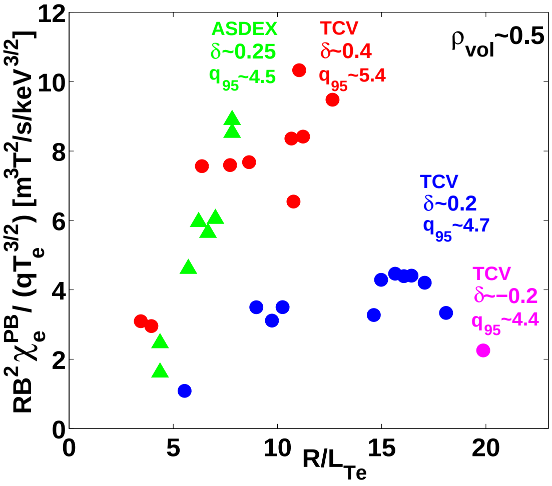

4. Shear modulation experiments with ECCD

Shear-modulation experiments have been performed by using two X2 clusters of 2 gyrotrons with 0.45MW each. The launchers are oriented toroidally for driving ECCD in opposite directions, and poloidally for having an identical deposition radius, r_{dep}. The power is switched on alternatively in the two beams for driving alternate ECCD at constant instantaneous ECH heating. Modulation frequencies from 5Hz to 70Hz have been used, but the analysis is mostly performed at the lowest frequency, using Thomson scattering data. The goal of the experiment is the study of the electron transport dependence on magnetic shear.

Because the modulated ECCD is localised in a narrow layer inside a conductive medium, the electrodynamic plasma response must be taken into account in estimating the actual current distribution. A model using magnetically coupled lumped circuits is applied for calculating the modulation amplitude of the current distribution, the main effect on shear being shown in Figure 6. The estimated modulation of the current density profile and shear (±40%) is supported by the evolution of the internal inductance, by voltage-current characteristic and sawteeth behaviour.

FIG. 6. Calculated magnetic shear profiles for co and counter-ECCD.

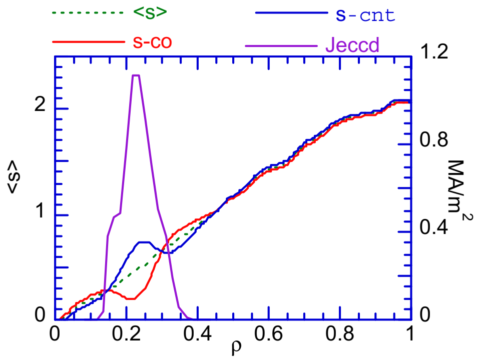

A striking feature is a strong oscillation in T_e, more than 30% peak-to-peak in the plasma core, in spite of constant input heating power. Small and negligible density oscillations are also observed, although a process different from energy confinement is acting on particles. The phase of the T_e oscillations confirms that the heat wave is generated inside r_{dep}, and propagates outwards.

FIG. 7. Average (dotted line), modulation (open squares) and relative modulation (full squares) amplitude of ∇T_e, relative heat flux modulation amplitude (solid line) (shot #24867).

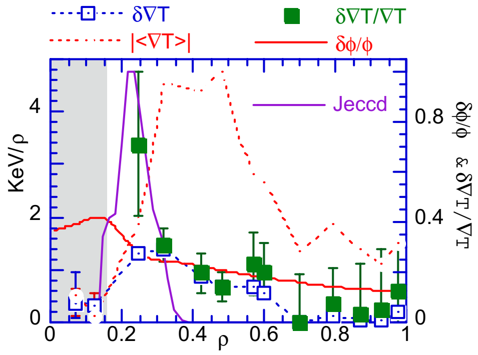

This oscillation can be interpreted as a change either in the thermal diffusivity χ_e or in the heat flux q_e, with an associated gradient modulation expressed as $\nabla\tilde{T}_e/\nabla T_e = \tilde{q}_e/q_e - \tilde{\chi}_e/\chi_e$. The main contribution to $\tilde{q}_e$ is the modulation of the ohmic power due to modulation of the resistivity and current density. Figure 7 shows that outside r_{dep}, $\tilde{q}_e/q_e$ compensates $\nabla\tilde{T}_e/\nabla T_e$, while at and inside r_{dep}, the gradient modulation can only be explained by a relative modulation of 40% of χ_e. This is confirmed by a local power balance, and is consistent with the 4% increase in the global energy content, taking into account the fact that only 25% of the volume is involved and that ohmic input is decreased when T_e is increased. The thermal diffusivity modulation is in phase with that of the magnetic shear; it decreases where the shear is low, and at all internal radii. The relative modulation in χ_e is of the same order of that estimated for the shear. This provides an important information on the issue of magnetic shear damping of drift-wave, fine-scale turbulence [10].

5. Electron internal transport barrier formation and control

FIG. 8. Time traces of typical eITB scenarios with an inductive current perturbation in the latter phase of the discharge to probe the eITB with an additional positive or negative j_{Ω} contribution.

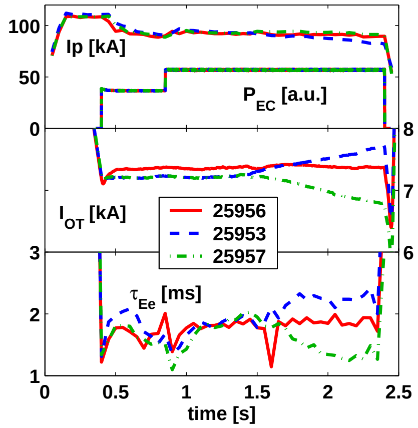

Electron internal transport barriers (eITB) have been extensively studied in the TCV tokamak, with an emphasis on steady-state scenarios. This is why the eITB presented are fully sustained by non-inductive currents, in our case by bootstrap current and ECCD. With the powerful and flexible ECCD system installed, the full plasma current can even be sustained non-inductively with off-axis beams only [11]. This allows the control of reverse shear scenarios in steady state.

FIG. 9. Thomson scattering pressure profiles corresponding to the discharges shown in Figure 8, time-averaged in the steady-state period [1.9s,2.35s], except for the open circles, averaged over [0.6s,0.8s]

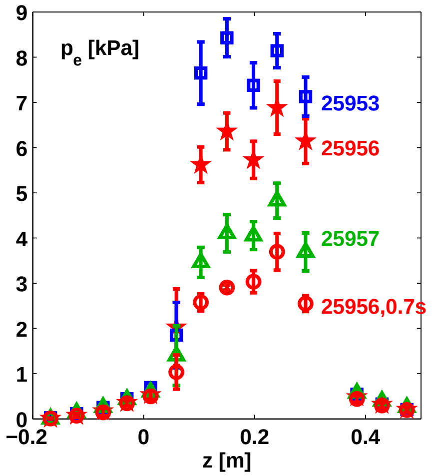

The usual scenario for our recent eITB physics studies is shown in Figure 8. First a stationary L-mode ohmic plasma is created, at low plasma current around $I_p = 90\text{kA}$. At 0.4s, two co-ECCD off-axis beams (0.9MW) are launched and the ohmic transformer current, I_{OT} is kept constant. Then the plasma evolves from a peaked, monotonic inductive current density profile j_{Ω} to a non-monotonic total profile fully sustained by j_{CD} plus j_{BS}, the ECCD and bootstrap current density profiles respectively [11]. This evolution occurs on the resistive current redistribution time, τ_{CRT} which is typically around 0.1-0.2s [12]. After that time, most of the inductive current has vanished and the safety factor, q attains a flat or reverse profile and the eITB forms rapidly, in less than 1ms [13][14]. One additional gyrotron (0.45MW) heating near the centre of the plasma is turned on at 0.8s. This enhances the eITB so that it can be clearly observed in the pressure profiles, as seen in Figure 9. Note that the global electron energy confinement time actually increases with this additional heating in the centre, Figure 8, since the power is deposited in an improved confinement region. It can be speculated that the microinstabilities have been stabilised and thus there is no longer any power degradation in the core.

FIG. 10. Time evolution of line integrated soft X-ray emissivity of select chords of the MPX

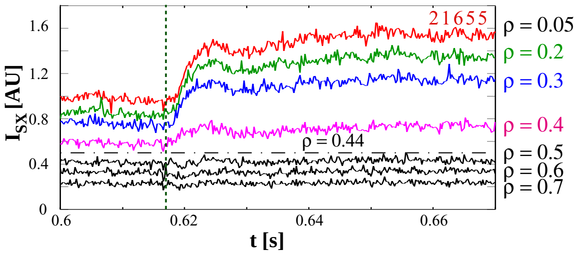

The barrier formation is best observed with the Multiwire Proportional X-Ray camera (MPX) with an appropriate high spatial and time resolution [15], Figure 10. The sudden increase in soft X-ray emissivity is dominated by an electron temperature increase. The radial location between chords with increasing and flat signals $\rho = 0.44$ corresponds to the barrier foot. The line integrated signal of chords viewing inside the barrier cannot be used to determine the effective rise time of the local temperature but the local emissivity profile may be obtained assuming a constant emissivity on a given flux surface and applying a minimum Fisher inversion method [16]. In the case shown in Figure 11, the eITB forms at $\rho = 0.3$ in a narrow region and the temperature rise then propagates rapidly inwards and outwards, with a characteristic time less than 1ms. This observation provides a unique test for validating theories on ITB.

FIG. 11. Inverted soft X-ray emissivity: a) profile snap shot plotted every 0.75 ms around ITB formation; b) temporal evolution at selected radial locations.

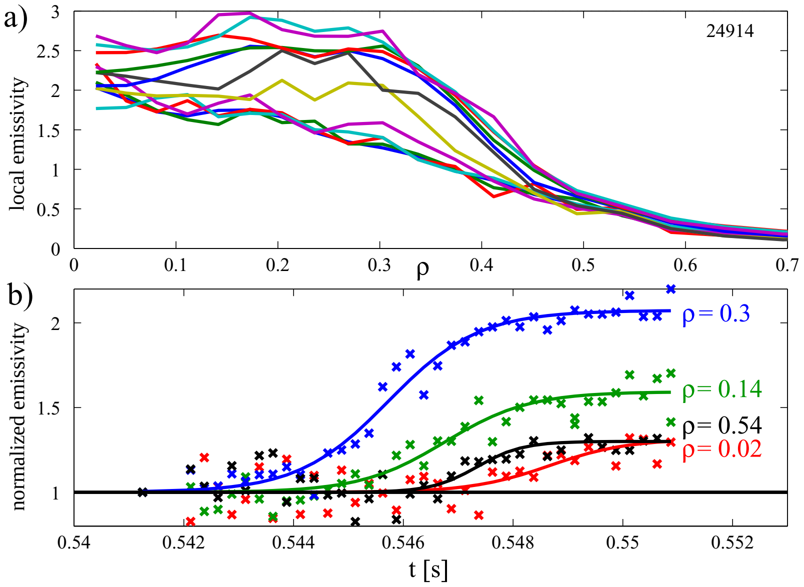

Once the discharge has reached steady-state, at 1.4s the waveform of I_{OT} is changed such that is induces a ±30mV constant surface loop voltage [17]. This drives an inductive current with a well-known profile that peaks on-axis within about one τ_{crt} and reaches steady-state in less than 1s. The additional ohmic power is negligible, ~3kW, as compared to the total EC power, 1.35MW, and even to the central ECH, 0.45MW. Then the effect of only perturbing the current profile, at constant input power can be tested. As clearly seen from Figure 8, the electron confinement time varies from ~1.4ms with +30mV and $I_p \cong 90\text{kA}$, to ~2.3ms with –30mV and $I_p \cong 70\text{kA}$. Since the total plasma current is higher with the additional inductive current, the effective confinement improvement, normalised to standard scaling laws, actually almost doubles between these two cases. This is confirmed by the pressure profiles shown in Figure 9.

FIG. 12. Time evolution of magnetic shear due to an imposed surface loop voltage perturbation of +30 mV on a plasma corresponding to the eITB discharges shown in Figure 8 at 1.4 s, with V_{loop}=0 over the whole minor radius.

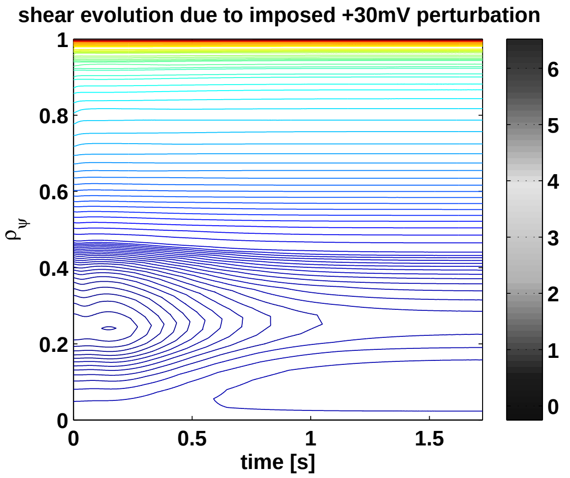

In Figure 12, we show the time evolution of the magnetic shear due to the addition of a loop voltage of +30 mV. The ASTRA code [18] is used, keeping everything else constant, in particular the transport coefficient [12]. First the reverse shear is slightly enhanced, since the positive inductive current density perturbation comes from the edge, and then the q profile becomes essentially monotonic. This transient behaviour, which lasts about 0.1-0.2 s, is actually observed with larger perturbations [19]. The final q profile is monotonic or flat with +30 mV, and much more reverse with –30 mV [12], corresponding to a degradation and an improvement of confinement respectively. Therefore these experiments show clearly that current profile is the primary cause for improved and anomalous electron transport in these eITB discharges. This is consistent with previous experiments where co- and counter-ECCD were added in the centre [20][21]. They are also consistent with global linear gyrokinetic simulations which show that TEM are the most unstable micro-instabilities in these discharges with T_e » T_i and their growth rate is strongly reduced when shear decreases and becomes negative [22]. These results are also obtained with GLF23 [8], which has been used within the ASTRA code to simulate self-consistently a similar discharge. The simulations confirm that reverse magnetic shear is sufficient to form an eITB, and the bootstrap current provides a significant contribution to create and maintain the non-monotonic current profile [23]. The simulations also show that it is difficult to determine if the confinement is improved in a small region around q_{min} or in the whole core region inside the foot of the barrier, since the central ECH beam is not localised enough. In any case, it is always better to heat in the centre to maximise the bootstrap fraction and the global electron thermal energy confinement time [23].

6. Third-harmonic, top-launch ECH

FIG. 13. View of the X3 top-launch mirror. The three RF beams are directed on one single focusing mirror with radial and poloidal steering capabilities. The poloidal angle can be controlled in real time. On the poloidal cross section, the maximum steering range is outlined in red.

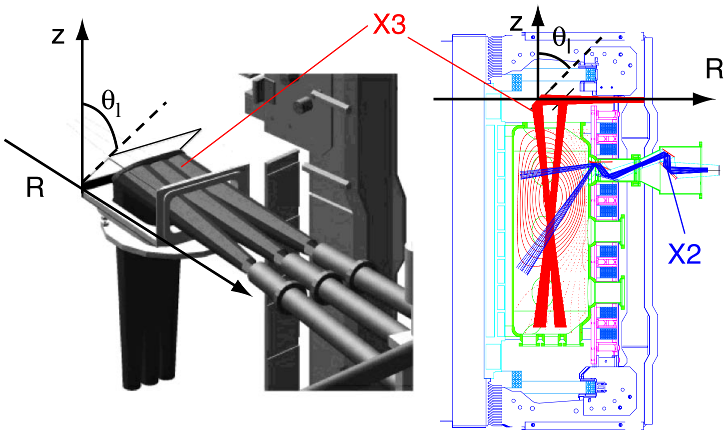

In the moderate magnetic field of TCV (1.5 T), the X3 system broadens the operational space with the possibility of heating plasmas at high density, well above the cutoff density of the X2 system ($4.2\times10^{19}\text{m}^{-3}$). To compensate for the weak absorption coefficient, top-launch injection is used that maximizes the ray path along the resonance layer, sketched in Figure 13. The main characteristic of this launching scheme is the sensitivity of the absorption to the poloidal injection angle, θ as it is shown in Figure 14, where, with 0.45 MW of injected power, the level of absorption is indicated by the variation of the central temperature deduced from the soft X-ray emission measurement along a central vertical viewing line [24].

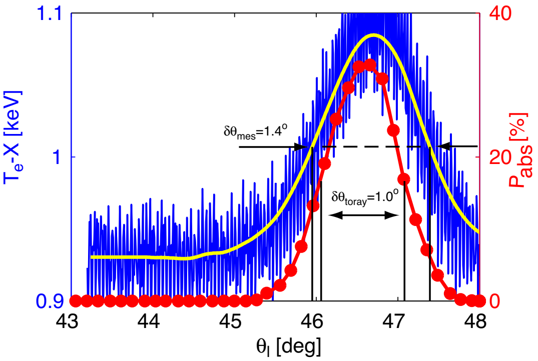

FIG. 14. Soft-X ray temperature versus poloidal injection angle θ (in blue). In red the predicted absorption calculated with the TORAY-GA code.

To maintain the maximum absorption in plasma discharges with unexpected variations of both density (refraction) and temperature (relativistic shift), a real time control of the injection angle has been developed. The feedback system consists in a synchronous demodulation of the plasma temperature response to a harmonic perturbation of the injection angle at 13 Hz. This produces a feedback signal which is proportional to the actual value of $dT_e/d\theta$ and the mirror is controlled to track the maximum of the absorption curve where this derivative is zero.

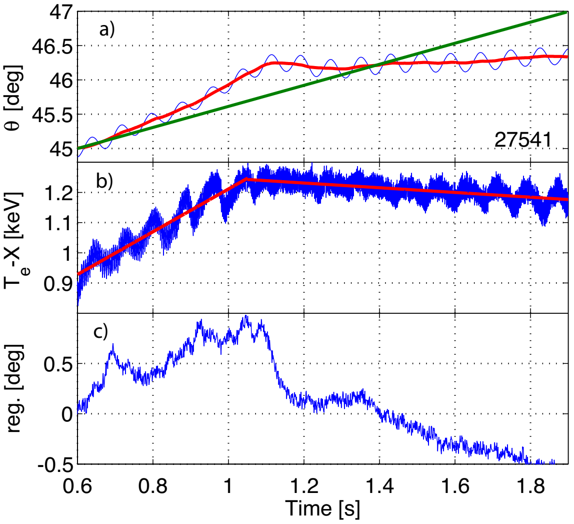

FIG. 15. a) Pre-programmed (green) and feedback controlled (red) mirror angle. b) Central plasma temperature. c) Error signal.

The capabilities of the feedback are presented in Figure 15 where the mirror poloidal angle was pre-programmed to perform a linear sweep crossing the maximum absorption. The feedback controlled mirror-angle reached the optimum angle faster than the pre-programmed sweep and then (t = 1.1 s) maintained this optimum angle despite the externally imposed ramp. A stable real-time optimisation of the injection angle has been obtained on a wide variety of L-mode plasmas and further development for H-modes are presently under way.

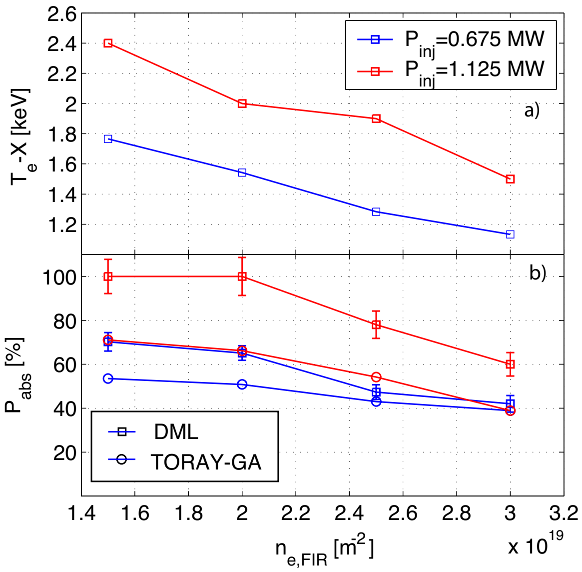

FIG. 16. a) Central temperature versus line integrated density for two levels of X3 injected power. The temperature of the ohmic target is 0.9keV. b) Absorbed fraction measured (DML squares) and predicted by TORAY-GA (circles).

The X3 absorption studies were significantly simplified with the real-time optimisation of the launcher. The absorbed fraction versus plasma density at different levels of the injected power are presented in Figure 16 with target plasma parameters: elongation 1.6, triangularity 0.1, $I_p = 230\text{kA}$. The absorbed power is measured using the response of the diamagnetic flux to a modulation of the injected power [25]. The difference between the measured absorbed fraction and that predicted by the TORAY-GA code is to be associated with the existence of a suprathermal population generated by the X3 wave itself. At higher electron densities this difference is lower since a fast thermalisation of the suprathermal population occurs. First comparisons between the absorption predicted by the ray tracing-code, TORAY-GA and the beam-tracing code have been made [26].

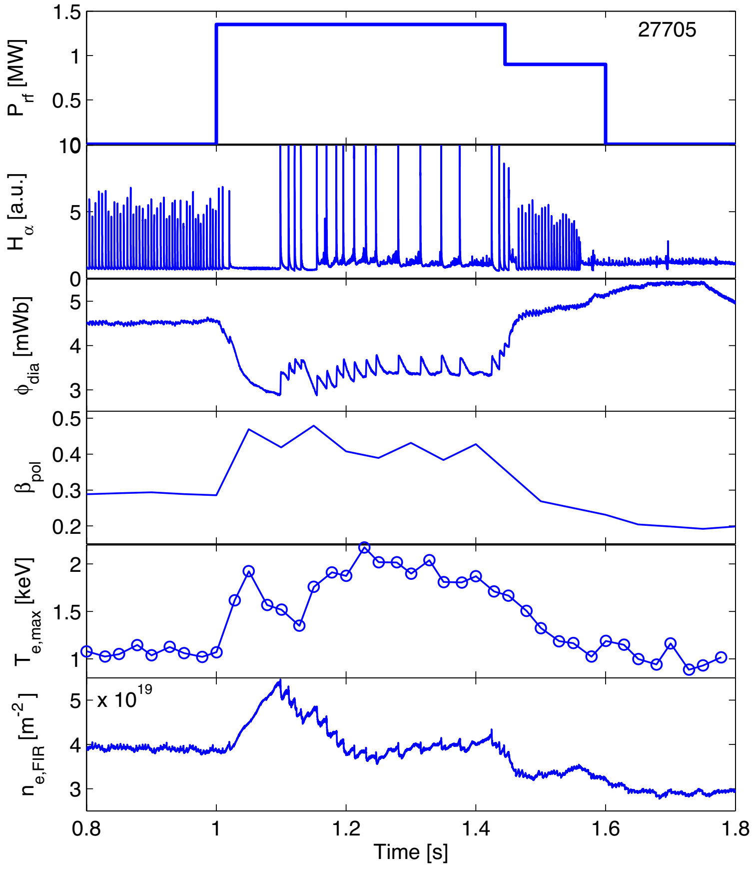

FIG. 17. Temporal evolution plasma parameters in a quasi-stationary ELMy H-mode with X3 heating, from top to bottom: injected X3 power, H_α emission, diamagnetic flux, poloidal β, central electron temperature, line averaged density.

Until X3 heating was installed on TCV the only routinely available ELMy H-modes were ohmic H-modes [27]. Initial results with low power X3 heating ($P_{X3} < P_\Omega$, where P_Ω is the ohmic power) applied to ELMy plasmas indicate that the ELM frequency decreases with increasing power but the ELM regime remains unchanged [28]. In recent experiments $P_{X3} \cong 3P_{\Omega}$ has been obtained and the effects are significantly different. Figure 17 shows the temporal evolution of a quasi-stationary ELMy H-mode plasma heated with 1.35 MW top launch X3. The ELM regime exhibits a clear transition at the application of the additional heating accompanied by a reduction in the ELM frequency and an increase by a factor 10 in the stored energy released at each ELM. At 1.42 s one of the X3 gyrotrons was switched off and the plasma immediately went back to the low power regime, indicating that there is a minimum additional heating power to maintain the large ELM regime.

7. H-mode Threshold Power with ECH

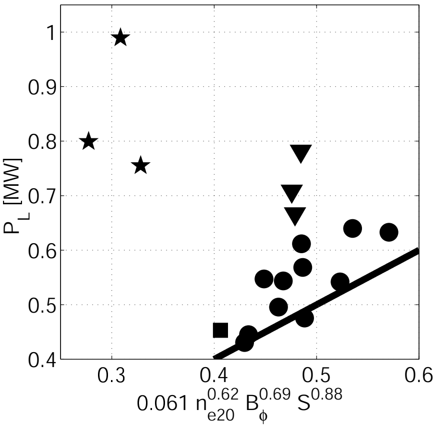

FIG. 18. LH transition power threshold for ohmic favourable (circles) and unfavourable (triangles) ion ∇B drift, X2 unfavourable (stars) and X3 favourable (square).

The LH threshold power was measured in discharges with additional ECH-X2 power. Only densities below the cut-off density were investigated. The LH transitions obtained in these conditions with an unfavourable ion ∇B drift exhibit a higher threshold power than the lowest ohmic threshold, Figure 18 (stars), in agreement with previous results showing that the threshold power increases with decreasing density below a given density [29]. The minimum in the threshold power is then located between the two groups of data. These experiments show that the threshold density can be lowered with the ECH but at the cost of more power. The TCV ECH-X3 system has a higher cut-off density, $11.5\times10^{19}\,\mathrm{m}^{-3}$, motivating an experiment to close the gap between the ohmic and ECH-X2 data. The mirror angle was slowly tilted during the heating pulse in order to vary the total interaction volume and thus the power absorption. An LH transition occurred when the absorbed power measured using modulation on the diamagnetic flux [25] reached approximately 0.2 MW (Figure 18, square). This X3-assisted LH transition was obtained at a power and a density in agreement with the ohmic LH transitions. This similarity suggests that the underlying transition physics does not depend on the heating scheme and that the increase in threshold power observed in the ECH-X2 data is a general property of the low density transitions. The minimum H-mode threshold power with favourable ion ∇B drift is 0.45 MW for this particular plasma shape, at a line averaged density of $4.5\times10^{19}\,\mathrm{m}^{-3}$.

8. Outlook

The powerful ECH system of TCV and its highly adaptable launching system are now fully deployed and have proved to be unique tools to achieve high performance regimes both in H-mode plasmas and in ITB scenarios. These capabilities can now be exploited to further optimise the performances of these plasmas and to pursue the investigations of the involved physical mechanisms in studies of fast particle generation and relaxation, heat transport and related turbulence modelling and detrimental instability mitigation.

Acknowledgment. This work was supported in part by the Swiss National Science Foundation.

References

[1] CODA, S., et al., Nucl. Fusion **43** (2003) 1361.

[2] CODA, S., et al., 30th EPS Conf. on Control. Fusion and Plasma Phys., 2003, St. Petersburg, Russian Federation, Europhys. Conf. Abstr. **27A** (2003) P-3.134.
[3] BLANCHARD, P., et al., Plasma Phys. Contr. Fusion **44** (2002) 2231.
[4] CAMENEN, Y., et al., 10th EU-US TTF Workshop, 2004, Varenna, Italy.
[5] POCHELON, A., et al., this conf., paper EX/P9-1.
[6] MORET, J.-M., et al., Phys. Rev. Lett. **79** (1997) 2057.
[7] POCHELON, A., et al., Nucl. Fusion **39** (1999) 1807.
[8] WALTZ, R.E., et al., Phys. Fluids B, **4** (1992) 3138.
[9] IMBEAUX, F., et al., Plasma Phys. Contr. Fusion **43** (2001) 1503.
[10] KENDL, A., SCOTT, B., 29th EPS Conf. on Plasma Phys. and Control. Fusion, 2002, Montreux, Switzerland, Europhys. Conf. Abstr. **26B** (2002) P-3.211.
[11] GOODMAN, T. P., et al, Nucl. Fusion **43** (2003) 1619.
[12] ZUCCA, C., et al, Varenna-Lausanne Theory Conference, 2004, Varenna, Italy.
[13] HENDERSON, M.A., et al., accepted in Phys. Rev. Lett.
[14] HENDERSON, M.A., et al, this conf., paper EX/P3-3.
[15] SUSHKOV A.V. et al., 29th EPS Conf. on Plasma Phys. and Control. Fusion, 2002, Montreux, Switzerland, Europhys. Conf. Abstr. **26B** (2002) P4-118.
[16] ANTON, M., et al., Plasma Phys. Contr. Fus. **38** (1996) 1849.
[17] GOODMAN, T. P., et al, 30th EPS Conf. on Control. Fusion and Plasma Phys., 2003, St. Petersburg, Russian Federation, Europhys. Conf. Abstr. **27A** (2003) P3-208.
[18] PEREVERZEV, G.V., et al., Max Planck - IPP Report, IPP 5/42 (1991).
[19] SAUTER, O., et al, submitted to Phys. Rev. Lett.
[20] HENDERSON, M.A., et al., Phys. Plasmas **10** (2003) 1796.
[21] HENDERSON, M.A., et al., Plasma Phys. Control. Fusion **46** (2004) A275.
[22] BOTTINO A., “Modelling of global electrostatic microinstabilities in tokamaks: effects of ExB flow and magnetic shear”, PhD Thesis, 2004, École Polytechnique Fédérale de Lausanne, Switzerland.
[23] FABLE, E., SAUTER, O., Varenna-Lausanne Theory Conference, 2004, Varenna, Italy.
[24] HOGGE, J.P., et al., Nucl. Fusion, **43** (2003) 1353.
[25] MANINI, A., et al., Plasma Phys. Control. Fusion, **44** (2002) 139.
[26] ALBERTI, S., et al., this conf., paper EX/P4-17.
[27] MARTIN, Y., et al., 18th IAEA Conf. on Fusion Energy, 2000, Sorrento, Italy, paper EXP/5-30.
[28] PORTE, L., et al., 19th IAEA Conf. on Fusion Energy, 2002, Lyon, France, paper EX/P5-15.
[29] FIELDING, S.J., et al., Plasma Phys. Control. Fusion **38** (1996) 1091.